The following publication Zhao, Z., & To, S. (2018). An investigation of resolved shear stress on activation of slip systems during ultraprecision rotary cutting of local anisotropic Ti-6Al-4V alloy: Models and experiments. International Journal of Machine Tools and Manufacture, 134, 69–78 is available at https://doi.org/10.1016/j.ijmachtools.2018.07.001.

An investigation of resolved shear stress on activation of slip systems during ultraprecision rotary cutting of local anisotropic Ti-6Al-4V alloy: models and experiments

ABSTRACT

Ti-6Al-4V alloy with local anisotropic characteristics is produced by electropulsing treatment (EPT) and used in ultraprecision rotary diamond cutting to explore the deformation mechanism of the alloy. Two different orientations of lamellar martensite α give rise to the local anisotropic behaviour. Critical resolved shear stress (CRSS) is introduced in this paper to investigate the slip modes of the hexagonal closest packing martensite. A geometrical and physical model is also proposed for calculation of resolved shear stresses on various slipping systems. The results show that glide occurs in some certain directions on the condition that resolved shear stress equals or exceeds the CRSS. The cutting force varies with martensitic orientations, which is supposedly due to the combined effects of lamellar α phase sizes and the coordination or competition of diverse slipping directions.

Keywords: Ti-6Al-4V alloy; Lamellar martensite; Anisotropic behaviour; CRSS; Ultraprecision rotary diamond cutting.

1. Introduction

In comparison to conventional machining, ultra-precision diamond turning of single crystals with low material removal rate is strongly affected by anisotropic behaviour. Experimental and theoretical research has been systematically conducted to investigate the influence of isotropic crystallographic orientation of single crystal metals on the cutting forces, chip morphologies, and surface roughness during ultra-precision machining [1-3]. For instance, periodic force fluctuation and symmetrical surface morphologies in certain crystal orientation has been observed in turning single crystal aluminium [4]. Some single crystal semiconducting materials, such as silicon and germanium, have also shown strong anisotropic properties in micro cutting processes [5, 6]. The critical undeformed chip thickness used to evaluate the machinability of these infrared semiconductors is strongly relevant to its crystallographic planes and orientations. Since the cutting depth of ultra-precision turning is in a range of several micrometres, which is usually smaller than the average grain size of polycrystals, one of the primary purposes of investigating single crystal metal or semiconductor turning is to provide valuable guidance for machining polycrystalline

materials that display isotropic properties due to the random distribution of a large number of grains with different orientations.

The high strength and low weight polycrystalline Ti-6Al-4V alloy has increasingly been applied in automotive, aerial and biomedical industries for its superior mechanical properties as well as exceptional biocompatibility [7]. Previous studies of this alloy with a microstructure of near equiaxed α grains distributed in β matrix concluded that the inherent nature of inferior thermal conductivity, chemical reaction at high temperature, and low modulus of elasticity restrict its machinability in both conventional and ultra-precision machining, giving rise to severe tool wear, high vibration, and low material removal rates [8-10]. Based on the inherent nature, several assist methods have been proposed to improve the machinability of Ti-6Al-4V alloys, such as laser-assisted machining [11], ultrasonic assisted turning [12] and magnetic field assisted cutting [13]. Furthermore, the cutting mechanism [14, 15] and material properties [16] in ultraprecision machining of Ti-6Al-4V alloys have also been investigated. Not only materials have effect on ultraprecision cutting process, but also the process greatly affects the surface microstructure evolution and mechanical properties of the Ti-6Al-4V alloy, which is explored and modelled from the viewpoints of dislocations and grain or subgrain boundaries [17].

Since the mechanical properties of Ti-6Al-4V alloy depend on its microstructures, a large amount of studies have been carried out to study the microstructure evolution after heat treatment and thermomechanical processing [18-20]. In comparison to the conventional annealing process, electropulsing treatment (EPT) is an efficient method to alter material microstructures, such as copper alloys [21], magnesium alloys [22] and zinc alloys [23]. Recently, investigations have also been conducted on studying the microstructure evolution of titanium alloys [24, 25]. Besides, the machinability of the titanium alloys after ETP have been investigated by both finite element method (FEM) and experiments in ultraprecision machining, and the authors found that the cutting forces and surface roughness could be improved after proper EPT process [16, 26].

Generally, three types of microstructures, i.e. equiaxed α grains and β phase, bimodal structures with primary α phase and α/β lamellas, and almost fully lamellar α structures, can be obtained from the manufacturing process. Polycrystalline Ti-6Al-4V alloys with equiaxed α grains and β phase and bimodal structures show no anisotropic behaviour during machining because of the arbitrary grain distribution, but Ti-6Al-4V alloy with different orientations of

lamellar α phase show significant anisotropic properties. Acicular martensite α with hexagonal close-packed (hcp) structure can be obtained through phase transformation from single β phase followed by water quench or selective laser melting techniques [27, 28]. At the beginning of the phase transformation process, martensite α lamellae form heterogeneously at prior β grain boundaries, resulting in an intermittent slender α layer on β grain boundaries. Then, α phase nucleates at the inner β grains grow into β grains and stop until they meet other α lamellar plantlets with different variant of the Burgers orientation relationship in the same β grain. Finally, α colonies with one or several orientations form in a single β grain [29, 30]. The orientation diversity usually leads to a local anisotropic property of Ti-6Al-4V alloy. Furthermore, the deformation mechanism is strongly affected by the crystallographic orientations for a selected plane, depending upon the difficulty of activation of slip systems [5, 31]. Critical resolved shear stress (CRSS) is frequently used to determine which slip or twin systems are activated during metal deformation [32-34]. Though numerous studies have been carried out to study the structure, orientations relationship and CRSS of martensitic α plantlets with hcp structure, little research has been conducted to investigate the influence of martensite orientation on the cutting force and explore the activation of slip or twin systems in the micro machining process. Hence, the purpose of this paper is to investigate the effect of martensitic orientations of Ti-6Al-4V alloy produced by electropulsing treatment on the cutting force variation and deformation mechanism in ultraprecision rotary diamond cutting.

2. Materials and experimental procedures

Commercial Ti-6Al-4V alloy (5.900% Al, 4.032% V, 0.075% Fe, 0.018% C, 0.030% N, 0.120% O, 0.001% H, balance Ti) with a diameter of 3 mm was utilized in micro rotary cutting. The EPT device (THDM-III, developed by Tsinghua University) is applied for producing high density current pulse to treat the Ti-6Al-4V alloy and a self-developed sample metal electrode is used to fix the samples, as shown in Fig. 1. The voltage and frequency of EPT were 40 V and 600 Hz respectively, a condition under which samples can be treated in single β phase, and water quench (WQ) was performed after EPT for 2 min. The original and EPT treated samples were subsequently cut into 4 pieces with a length of 6 mm, followed by mechanical grinding and polishing for the final micro rotary cutting.

Fig. 1 EPT device of (a) front view, (b) back view and (c) self-developed sample fixture

The nose radius, rake angle and front clearance of the single crystal diamond tool are 1.567 mm, 0° and 12.5°, respectively. Rough turning was firstly conducted in order to obtain a flat surface, and rotary cutting with a low spindle speed of 60 rpm and cutting depth of 4 μm was carried out subsequently on an ultra-precision machine (Moore Nanotech 350FG). An outside-in cutting approach was adopted during the rotary cutting process and 4 grooves with an interval of 0.2 mm were obtained after machining. A Kistler 9256C1 force sensor was installed below the cutting tool to measure the cutting forces. The metallographic microstructure was obtained from a DFC 450 optical microscope (LEICA). White light interferometers (Wyko NT8000 and Zygo Lamda Nexview) were applied to observe the topographies of the machined surface. Microstructure evolution was measured by the Hitachi S4800 scanning electron microscope (SEM) equipped with an electron backscattered diffraction patterns (EBSD) system. Ion milling (HITACHI Ion Milling System IM4000) was performed on the samples to eliminate residual stress on the surface layer induced by mechanical grinding and polishing, for obtaining high quality Kikuchi patterns during EBSD measurement. As for the analysis of microstructure of chips, a precision ion polishing system PIPS (Gatan 691) was employed to penetrate the chips for observation of topographies by a transmission electron microscope (TEM, JEOL Model JEM-2011).

3. Resolved shear stress model on different slip systems

Shear deformation occurs only when the resolved shear stress applied on the slip systems equals or exceeds the corresponding CRSS, because dislocations in metals cannot migrate if the resolved shear stresses do not reach the CRSS. According to the geometrical relationship in Fig. 2 (b), the resolved shear stress σ_s obtained from parallel and vertical component stresses on one direction of slip systems can be expressed as follows:

$$\sigma_s = \sigma_l(|cos\theta cos\omega_{1i} + sin\theta cos\omega_{2i}|) \quad (1)$$

where σ_l is the local shear stress applied on martensitic planes, θ is an angle between local shear stress direction and longitudinal direction of martensite, ω_{1i} and ω_{2i} are angles between slipping directions and martensitic longitudinal direction and transverse direction, respectively. Due to the symmetric characteristic of the hcp structure, the values of *i* can be 1, 2 and 3, representing three particular slipping directions on various slip planes. The stresses applied on the shear plane mainly include three parts, namely main shear stress (σ) caused by the comprehensive effect of cutting force and thrust force, resistance shear stress (σ_r) induced by the internal dislocation movement resistance, and drag stress (σ_d) on the motion of

dislocation, as shown in Fig. 2 (a). Hence, the resultant shear stress on the shear plane is given by:

$$\sigma_l = \sigma - \sigma_r - \sigma_d \tag{2}$$

The main shear stress calculation is simply obtained from the following geometrical relationship:

$$\sigma = \frac{F_c cos\varphi - F_t sin\varphi}{A_s} \tag{3}$$

where φ is the shear band angle measured from the SEM image, A_s is the plane area of the shear band, and F_c, F_f represent the main cutting force and thrust force, respectively. The internal resistance shear stress always results from the combination effect of grain/phase boundaries and dislocation forests, so the equation is modelled as follows [35]:

$$\sigma_r = \sigma_g + \sigma_\rho = \frac{\alpha_g \mu \sqrt{b}}{\sqrt{D}} + \alpha_\rho \mu b \sqrt{\rho} \tag{4}$$

where α_g, α_ρ are numerical constants which correlate to the internal strength of grain/phase boundary and dislocation forests, μ is shear modulus related to temperature in primary cutting zone, b is the magnitude of the Burgers vector, D is the average grain/phase size and ρ is dislocation density. Furthermore, metal deformation is also affected by the drag effect during machining under high strain rates deformation (>10^3 s^{-1}), which could also introduce a drag stress on the migration of dislocation. The equation is given by [35]:

$$\sigma_d = \alpha_d \dot{\varepsilon} \tag{5}$$

where α_d is the dislocation drag coefficient and $\dot{\varepsilon}$ is strain rate during the formation of cutting chips. The strain rate $\dot{\varepsilon}$ is correlated with the strain (ε) and frequency of serrated chip generation and expressed by [36]:

$$\dot{\varepsilon} = \varepsilon \times f \tag{6}$$

The shear strain ε within a serrated chip is given by:

$$\varepsilon = \frac{sin\chi}{sin\varphi \sin(\varphi + \chi)} \tag{7}$$

where χ is an angle between one side of serrated chip and normal direction of free chip surface. Furthermore, frequency f is given by:

$$f = \frac{2\pi R v}{d_c} \tag{8}$$

where R is the diameter of rotary cutting, v is the spindle speed and d_c is the distance between two neighbouring serrated chips.

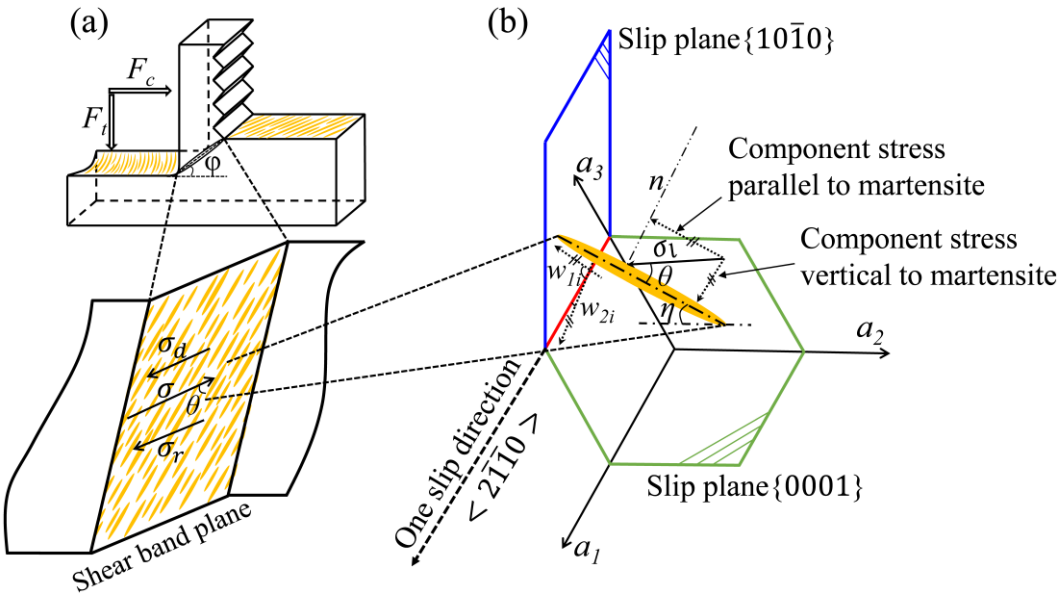

Fig. 2 (a) Stresses distribution on shear plane and (b) geometrical relationship of resolved shear stress on one slip direction of the hcp crystal structure

The angle ω is determined by the preferential orientation <u v t w> of martensite (longitudinal direction) and slipping direction <a b c d> of particular slipping systems, and it is simply calculated by the relationship between the two vectors. Similarly, the angle between martensitic transverse direction perpendicular to the preferential orientation and slipping direction in the same plane can also be obtained by the same calculation. What is worth noticing is that the calculation should be under the Cartesian coordinate system instead of four-axis coordinate system of hcp materials. The conversion formula follows the equation:

$$\begin{bmatrix} h' & u' \\ k' & v' \\ l' & w' \end{bmatrix} = \begin{bmatrix} 2h+k & \frac{\sqrt{3}(2u+v)}{2} \\ \sqrt{3}k & \frac{3v}{2} \\ \frac{\sqrt{3}a}{c} & \frac{c}{a} \end{bmatrix} \tag{9}$$

where <h' k' l'>, <u' v' w'> and <h k i l>, <u v t w> are the crystal planes and directions in the Cartesian and four-axis coordinate systems, respectively. The longitudinal direction of martensite is the favourable orientation <u v t w> of primary martensite both in region I and region III, which is similar to the microstructural distribution in materials with texture. Hence, the special martensitic {h k i l} planes and <u v t w> orientations in hcp materials can be calculated via the crystal orientation matrix, as follows [37]. The {h k i l} plane is

$$\begin{bmatrix} h \\ k \\ i \\ l \end{bmatrix} = \begin{bmatrix} \frac{\sqrt{3}}{2} & -\frac{1}{2} & 0 \\ 0 & 1 & 0 \\ -\frac{\sqrt{3}}{2} & -\frac{1}{2} & 0 \\ 0 & 0 & \frac{c}{a} \end{bmatrix} \begin{bmatrix} -sin\varphi_2 sin\varphi \\ cos\varphi_2 sin\varphi \\ cos\varphi \end{bmatrix} \quad (10)$$

and the corresponding <u v t w> crystal direction is

$$\begin{bmatrix} u \\ v \\ t \\ w \end{bmatrix} = \begin{bmatrix} \frac{2}{3} & -\frac{1}{3} & 0 \\ 0 & \frac{2}{3} & 0 \\ -\frac{2}{3} & -\frac{1}{3} & 0 \\ 0 & 0 & \frac{c}{a} \end{bmatrix} \begin{bmatrix} cos\varphi_1 cos\varphi_2 - sin\varphi_1 sin\varphi_2 cos\varphi \\ -cos\varphi_1 sin\varphi_2 - sin\varphi_1 cos\varphi_2 cos\varphi \\ sins\varphi_1 sin\varphi \end{bmatrix} \quad (11)$$

where $\varphi_1, \varphi \; and \; \varphi_2$ are the Euler angles in accordance with the Bunge's system, obtaining from the EBSD measurement. Then, the resolved shear stress on slipping systems can be written by:

$$\sigma_c = (\frac{F_c cos\varphi - F_f sin\varphi}{A_s} - \frac{\alpha_g \mu \sqrt{b}}{\sqrt{D}} - \alpha_\rho \mu b \sqrt{\rho} - \frac{2\pi \alpha_d R v sin\chi}{d_c sin\varphi sin\,(\varphi+\chi)})(sin\theta cos\omega_{1i} + cos\theta cos\omega_{2i}) \quad (12)$$

Furthermore, angles between cutting surface planes and various slipping or twining planes are also needed to be calculated in order to determine which slip systems are activated during ultraprecision rotary cutting. These angles η can be expressed by a well-known crystallographic formula in hcp materials, as follow [38]:

$$cos\,\eta = \frac{h_1 h_2 + k_1 k_2 + \frac{1}{2}(h_1 k_2 + h_2 k_1) + \frac{3a^2}{4c^2} l_1 l_2}{\sqrt{(h_1^2 + k_1^2 + h_1 k_1 + \frac{3a^2}{4c^2} l_1^2)(h_2^2 + k_2^2 + h_2 k_2 + \frac{3a^2}{4c^2} l_2^2)}} \quad (13)$$

where $\{h_1\; k_1\; i_1\; l_1\}$ and $\{h_2\; k_2\; i_2\; l_2\}$ are planes of calculated cutting surface planes and slipping or twining planes, respectively.

For the titanium alloys with hcp structure, the resolved shear stress on different slipping or twining systems can be calculated from equation (12), and the activated planes can be determined by equation (13). When the resolved shear stress on one slip system exceeds its corresponding CRSS, glide will occur instantly.

4. Results and discussion

4.1 Material's microstructure and cutting forces

Fig. 3 illustrates SEM morphologies of the workpiece after rotary machining of the original and EPT treated alloys followed by chemical etching. In Fig. 3 (a) and (b), four cutting grooves and cutting sequences of both samples are clearly shown in each of the machined surfaces. The microstructure of the original samples is given in Fig. 3 (c), composing of α matrix and β grains with an average size of about 0.7 μm. Fig. 3 (d) shows the amplifying morphologies of EPT treated samples obtained from the rectangular mark in Fig. 3 (b), and the microstructure is mainly constituted of martensite α with lamellar structures. Besides, some corrosion piths are observed from the morphologies of both samples due to the etching, but it has no influence on result analysis.

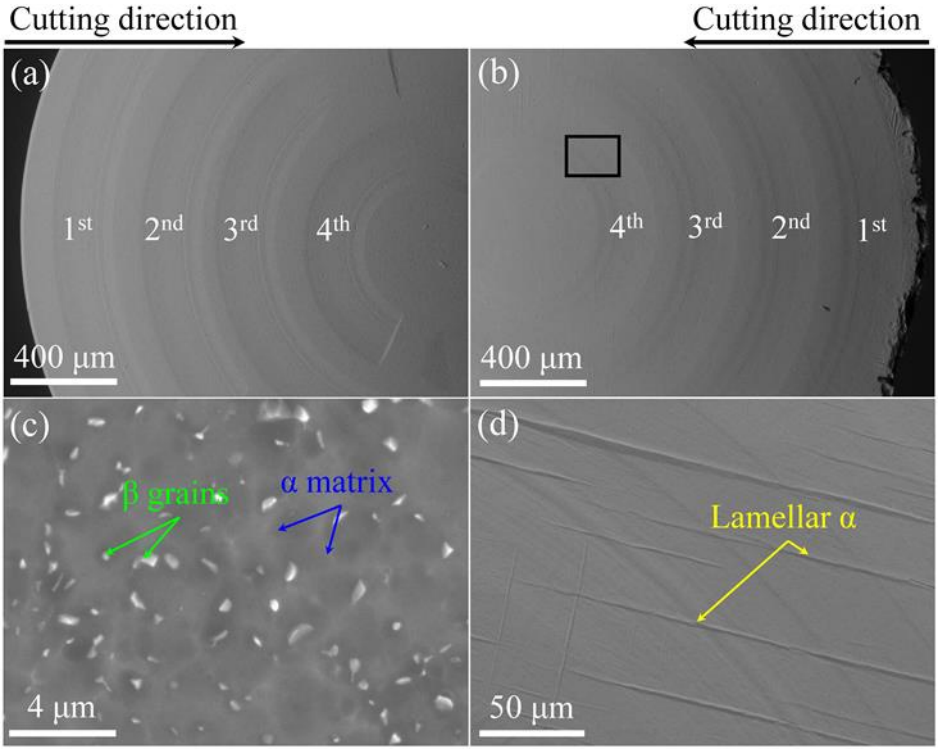

Fig. 3 Surface morphologies of (a) original and (b) EPT treated samples after rotary diamond turning, and the corresponding microstructures (c) and (d)

The cutting force variations from the first groove to the fourth groove of the original and EPT treated samples are shown in Fig. 4. With the diamond tool shifting to the centre, the average cutting force reduces from about 2.57 N to 2.34 N and from 3.04 N to 2.35 N for original samples and EPT treated samples, respectively. Since the spindle speed remains unchanged, the cutting speed decreases as the diamond tool moves from the outside to the inside of the workpiece. Therefore, the average cutting forces show a downward trend with the decreasing of cutting speeds in the low speed rotary cutting. Besides, the overall cutting forces of samples after EPT are slightly higher than that of the original samples, which is supposed to

be caused by the enhanced yield strength after the microstructure transfers from β grains in α matrix to α lamellar structure [39]. In addition, unlike samples without treatment that show stable cutting force evolution, the cutting force fluctuates in each corresponding groove of EPT treated samples due to the different martensitic orientations.

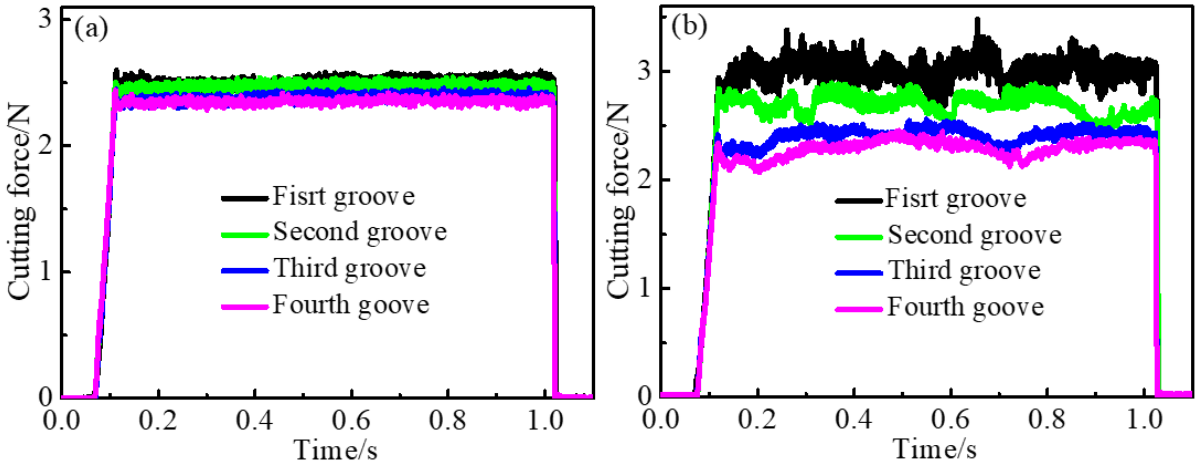

Fig. 4 Cutting force variations of different cutting grooves of (a) original samples and (b) EPT treated samples

In order to study the effect of martensitic orientations on the cutting forces, one part of the third groove with local anisotropic characteristic is selected as an example to investigate the cutting force variation. The morphologies in the rectangular marks of region I, II and II shown in Fig. 5 (a) correspond to the microstructures of Fig. 5 (b), (c) and (d), respectively. Two different orientations of lamellar martensite α are clearly seen from the magnifying morphologies. These two types of martensitic structures give rise to a local anisotropic characteristic of Ti-6Al-4V alloy, which can be reflected from the cutting force variation given in Fig. 6. The average cutting force of the original samples remains stable during the whole cutting process, while the cutting force of the EPT treated samples varies with different orientation of α at the three regions. At region I, the cutting force fluctuates with the forward motion of cutting tool and reaches the highest value at position A where the cutting direction tilts about 83° to most of the martensite α, then the cutting force gradually decreases after the diamond tool goes through the transition region II distributing orthogonal martensite α structure. Finally, the main cutting force increases to about 2.4 N and fluctuates significantly at region III.

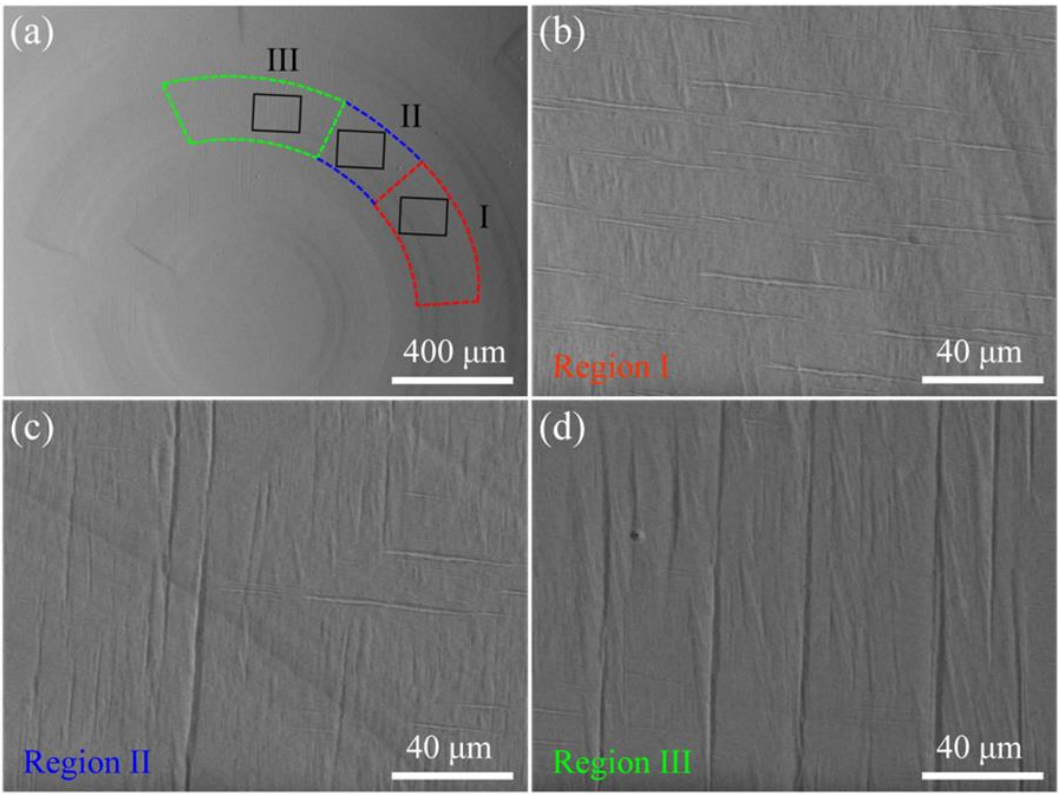

Fig. 5 Microstructure of local martensite in the third groove

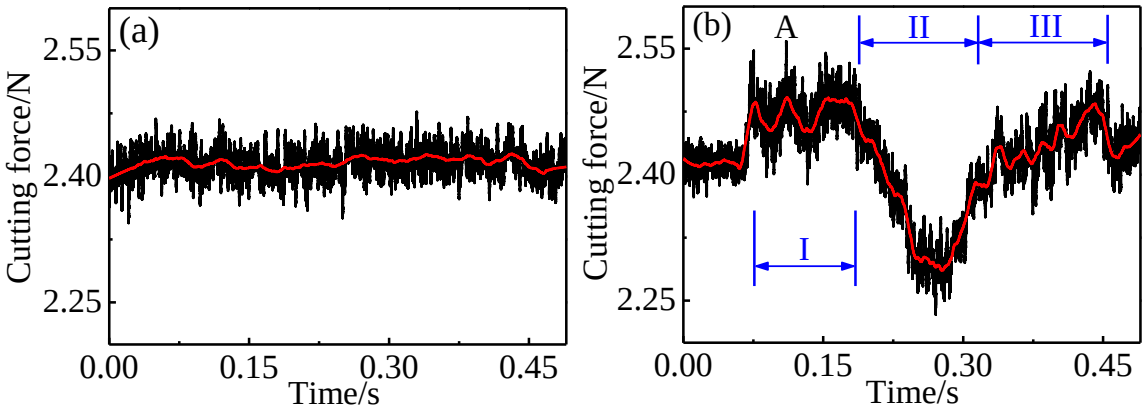

Fig. 6 Cutting forces variation of (a) original samples and (b) EPT treated samples in the three regions of the third groove

The microstructure of martensite α directly affects the cutting force of EPT treated samples with different orientation and thickness. Fig. 7 shows the three-dimensional (3D) topography features of the three regions, which was measured by the Zygo software Mx. The transition area from region I to region III can also be observed in Fig.7 (b), similar to the morphology in Fig. 5. The regional surface roughness S_a and peak-to-valley (PV) value of region I, featuring almost one direction of martensite α lamellae, are much smaller than those in region III with another direction of martensite α distribution. As the cutting depth is the same during the

whole cutting, different S_a and PV values indicate that the height fluctuation of lamellar α varies in the three cutting regions. From the profiles shown in Fig. 7 (d), the width and height of lamellar α are distinctly unequal in different regions, reaching an average width of about 4 μm and height of 95.8 nm in region I, and 6 μm and 398.6 nm in region III. The main cutting force in region I only shows a little higher (2%) than that of region III, which indicates that the cutting force decreases with martensite α size increase. However, this phenomenon is not fully in accordance with the Hall-Petch relationship where the yield stress should be inversely proportional to the square root of martensitic size. This may be due to the effects of various slipping behaviour in the two regions, which is explored in detail in the next section.

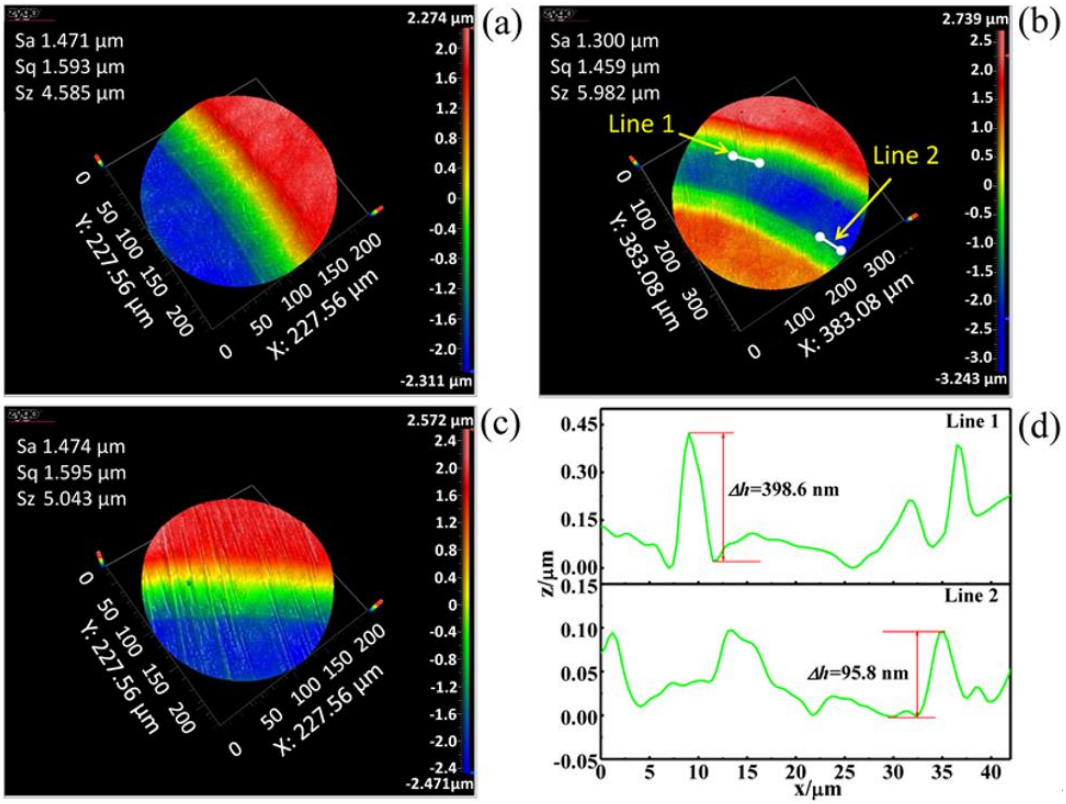

Fig. 7 Three-dimensional surface topographies of (a) region I, (b) region II, (c) region III and (d) height of two types of martensite

In order to confirm the effect of martensite α on cutting forces with different orientation and thickness, more than one pass was conducted under the same spindle speed and feed rate. As shown in Fig. 8 (a), two types of martensite α processing diverse features are observed (Region A and B). The fourth to sixth tool passes correspond to the same martensitic microstructure marked in Region A where the diamond tool has nearly the same contacting condition on the samples, so the main cutting forces show almost the same variation trend. Similar cutting force variations can also be found in Region B with a different martensitic

orientation. The periodic cutting force fluctuations further suggest that the α distribution has a significant effect on the cutting forces.

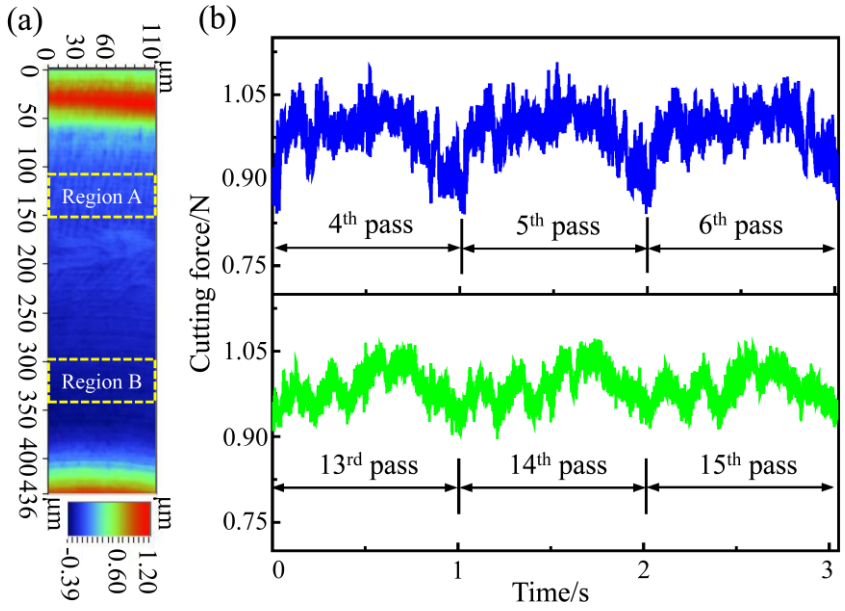

Fig. 8 Diamond turning Ti-6Al-4V with different martensitic structure: (a) surface topography measured by Wyko and (b) corresponding cutting forces in Region A (blue curve) and Region B (green curve)

4.2 Chip formation

Fig. 9 shows the chip morphology of the third cutting grooves of EPT treated samples. Serrated chips were obtained under a low cutting speed (about 4.21 mm/s), which is similar to the patterns in conventional machining. In Fig. 9 (a), the average shear angle φ and bulge angle χ of serrated chips were measured simultaneously, about 24.2° and 40.7°, respectively. Meanwhile, the average interval spacing d_c=1.5 μm was acquired from the magnified chips shown in Fig. 9 (b).

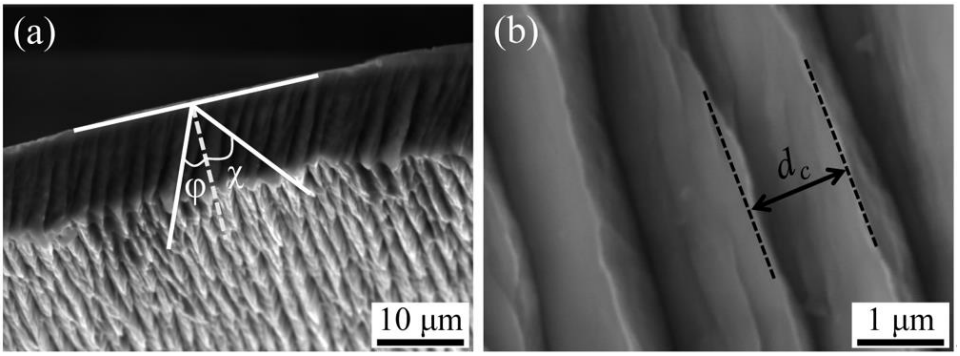

Fig. 9 Serrated chips pattern measured by SEM

4.3 Deformation mechanism and modelling

4.3.1 Deformation manner

The phase composition of Ti-6Al-4V alloy after EPT followed by WQ is given in Fig. 10. The EBSD data show that the microstructure consists of α phase with hcp crystal structure, and only 0.4% β phase with cubic crystal structure was found at the surface of the sample. Therefore, β phase can be neglected when analysing the deformation manners of ultraprecision rotary cutting of Ti-6Al-4V alloy. This means that the samples can be treated as titanium alloy with only hcp crystal structure. As for the deformation of hcp titanium, <a> slip of prismatic plane $\{10\bar{1}0\}$, basal plane $\{0001\}$ and pyramidal plane $\{10\bar{1}1\}$ with the same slipping direction of $< 11\bar{2}0 >$, <c+a> slip of pyramidal plane $\{10\bar{1}1\}$ with direction of $< 11\bar{2}3 >$ and tension or compression twinning are the main deformation mechanisms [40, 41]. Prismatic deformation of $\{10\bar{1}0\} < 11\bar{2}0 >$ is generally the most likely to be activated among these systems.

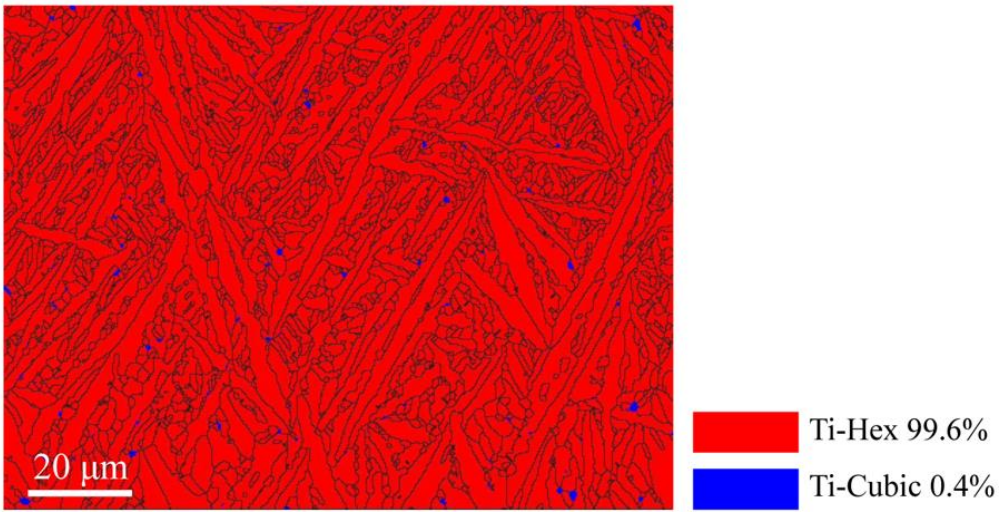

Fig. 10 Phase composition in a randomly selected area of region I

4.3.2 Primary slip mechanism in Region I

Fig. 11 presents the optical microstructure and inverse pole figure (IPF) orientation mapping in the same selected area of Fig. 10. As shown in Fig. 11 (a) and (b), the diamond tool starts to contact with martensite at θ=68° and ends with an angle of 112° in region I, while the angles in region III are 70° and 110°, respectively. In Fig. 11 (c), the triangular colour legend gives a standard crystal orientation of IPF mapping. Hence, the crystal plane (cutting surface) and favourable orientation (red colour) of α phase in region I can be obtained from IPF mapping. Furthermore, as the prevailing martensitic orientation in region III is parallel to that

in region I with green colour, the crystal plane and favourable orientation of martensite α can also be derived from the IPF mapping.

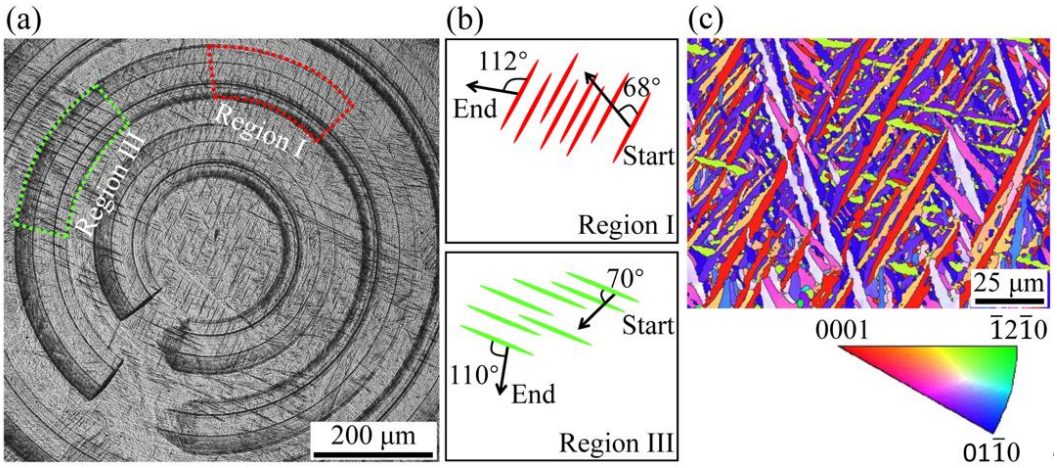

Fig. 11 EPT treated samples: (a) metallographic structure, (b) schematic diagram of starting cutting angles and end angles and (c) IPF mapping of a selected area in region I

In region I, the calculated tilt angle between cutting plane and basal plane is about 11°, as shown in Fig. 12 (a), so the <a> slip of basal plane is expected to be activated during the cutting process. Because <a> slip has three slipping directions, i.e. $[\bar{2}110], [11\bar{2}0]$ and $[1\bar{2}10]$, investigation should be conducted to explore which slipping direction is activated. Since the longitudinal and transverse directions of martensite can be obtained from the crystal orientation matrix, the angles w_{1i} and w_{2i} between the two directions and three different slipping directions can be calculated. The angles and other parameters to model the resolved shear stresses are tabulated in Table 1 and Table 2.

Table 1 Angles between shear stress direction and longitudinal and transverse directions

Basal <a> slips	$[\bar{2}110]$	$[11\bar{2}0]$	$[1\bar{2}10]$
w_{1i}	11.08°	49.95°	70.25°
w_{2i}	98.99°	40.88°	155.83°

Table 2 Material parameters from other references

Parameter	Value	Ref.
α_g	0.4544	[35]
α_ρ	0.5	[35]
α_d(kPa s)	4.5	[42]

μ(GPa)	48.66-0.032223T	[35]
b(m^{-1})	2.95×10^{-10}	[43]
ρ(m^{-2})	10^{12}	[33]

The cutting forces vary from 2.39 N to 2.55 N in region I, corresponding to thrust forces from 2.38 N to 2.49 N. A normal cutting temperature ranging from 300 K to 1000 K was considered in rotary cutting with low cutting speed. Normally, the forces decrease with temperature increase, but the exact relationship between force and temperature is not prone to be acquired. Therefore, the minimum and maximum resolved shear stresses on different slipping directions are investigated to explore the deformation mechanisms. According to the equation (12), stresses on the basal <a> slip system can be expressed by:

$$\begin{bmatrix}\sigma_{[\bar{2}110]}\\ \sigma_{[11\bar{2}0]}\\ \sigma_{[1\bar{2}10]}\end{bmatrix} = (493.23\sim575.98)\begin{bmatrix}|0.981cos\theta - 0.156sin\theta|\\ |0.643cos\theta + 0.756sin\theta|\\ |0.338cos\theta - 0.912sin\theta|\end{bmatrix} \quad (13)$$

where $\sigma_{[\bar{2}110]}$, $\sigma_{[11\bar{2}0]}$ and $\sigma_{[1\bar{2}10]}$ are resolved stresses on basal slipping directions of $[\bar{2}110]$, $[11\bar{2}0]$ and $[1\bar{2}10]$, respectively. The modelling curves of resolved shear stresses versus angle θ for the basal <a> slip with three slipping directions are shown in Fig. 12 (b). The preferential orientation marked by yellow arrow in Fig. 12 (a) can be obtained from equation (11). According to the investigation of CRSS on different slip systems, the CRSS for <a> slip on basal plane is about 444 MPa [33], as shown with dash red line in Fig. 12 (b). The angle θ between cutting direction and martensitic preferential orientation in region I starts with about 68° and ends with about 110°. At the beginning of this range, the average resolved shear stress in the $[11\bar{2}0]$ direction is the highest in comparison with the other two directions, so the slip is most likely to occur first in this direction. At the angle of about 81°, the average resolved shear stresses are equal to each other in the directions of $[11\bar{2}0]$ and $[1\bar{2}10]$. As mentioned above, the cutting force reaches its highest value near this angle and it is considered to be induced by the slip competition between the two slip directions. Slip $[1\bar{2}10]$ would then be activated after this angle. However, the resolved shear stress in $[\bar{2}110]$ direction is consistently smaller than the CRSS, so slip in this direction cannot be activated in this angle range.

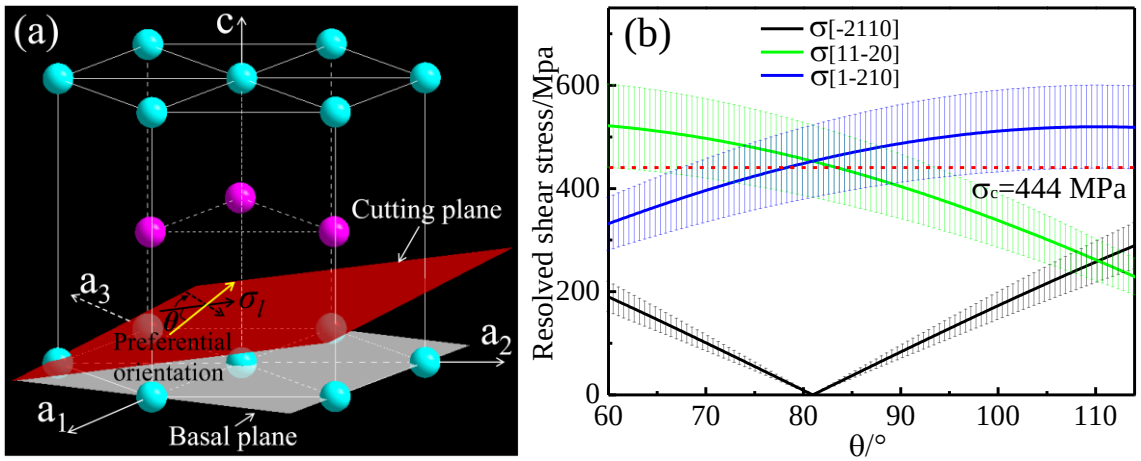

Fig. 12 (a) Crystal plane of cutting surface deviated from basal plane and (b) resolved shear stresses on different slip direction of basal <a> slip

4.3.3 Deformation mechanisms in Region III

Fig. 13 (a) geometrically shows the cutting surface plane (green colour) in region III. The resolved shear stresses calculation is similar to that in region I, and the stresses on prismatic <a> slip, pyramidal <c+a> slip, and three twinning systems are illustrated in Fig. 13 (b)-(f). The CRSS of prismatic <a> slip and pyramidal <c+a> slip for polycrystalline Ti-6Al-4V alloy is about 380 MPa and 631 MPa, respectively [33]. Therefore, activation of prismatic plane with slipping directions of $[\bar{2}110]$ and $[1\bar{2}10]$ is the primary deformation mechanism when the diamond tool passes through region III, and no pyramidal <c+a> slip occurs because the resolved stress cannot reach its CRSS.

For twinning deformation, the CRSS is close to the basal slip, namely, about 444 MPa. Fig. 13 (d)-(f) gives the resolved shear stresses on the $\{10\bar{1}2\} < 10\bar{1}1 >$, $\{11\bar{2}1\} < \bar{1}\bar{1}26 >$ and $\{10\bar{1}1\} < \bar{1}012 >$ twin systems. The results indicate that only $\{10\bar{1}2\} < 10\bar{1}1 >$ type of twin could be activated after the angle is larger than 106°. Therefore, deformation behaviour in a manner of twinning should only own a few portion of the total deformation in ultraprecision rotary cutting region III.

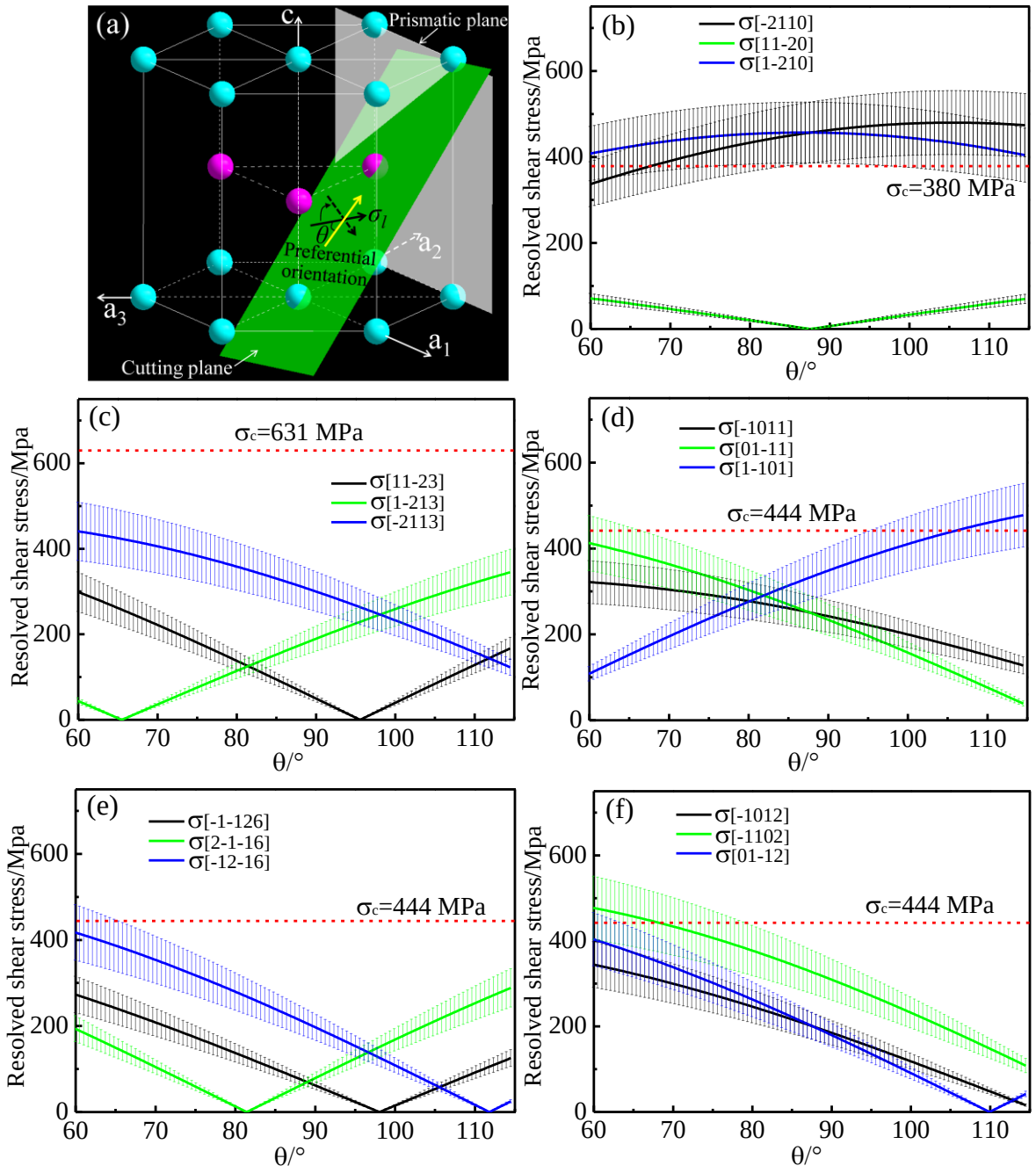

Fig. 13 (a) Crystal plane of cutting surface deviation and resolved shear stresses on (b) prismatic <a> slip, (c) pyramidal <c+a> slip, (d) $\{10\bar{1}2\}<10\bar{1}1>$ twins, (e) $\{11\bar{2}1\}<\bar{1}\bar{1}26>$ twins and (f) $\{10\bar{1}1\}<\bar{1}012>$ twins

The TEM bright field morphologies shown in Fig. 14 support the twinning deformation mechanism of region III. The microstructure is composed of lamellar martensite before rotary cutting, as shown in Fig. 14 (a), while the phase was smashed into extremely small equiaxed grains with an average size of about 5 nm after cutting. Among these grains, a small amount of deformation nanotwins were also clearly observed in Fig. 14 (b), which is supposed to happen after the resolved shear stress exceeds the corresponding CRSS.

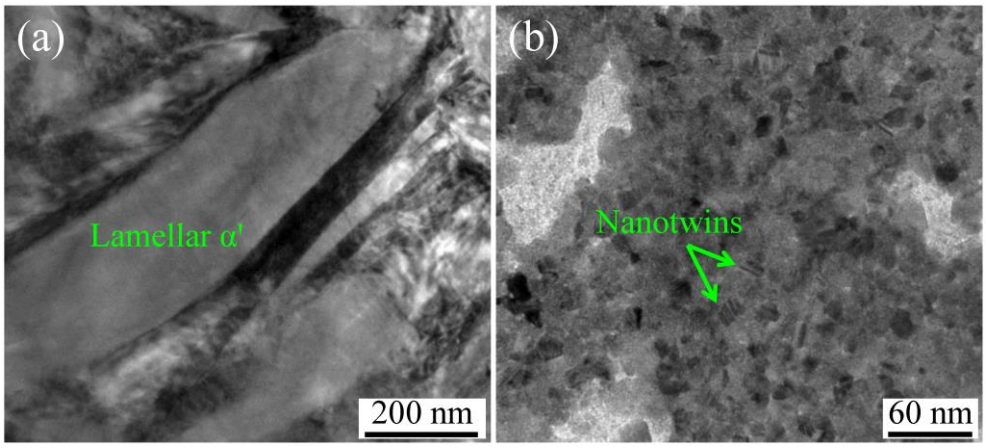

Fig. 14 TEM morphologies of (a) EPT treated Ti-6Al-4V alloy and (b) chips after ultraprecision rotary cutting

Furthermore, the domain deformation mechanism in region III is a type of prismatic <a> slip which is easier to glide than that of <a> slip of basal plane in region I, so this might account for why the average cutting force is not fully in agreement with the Hall-Petch relationship. Moreover, the formation of serrated chips was supposed to be one reason resulting in cutting force variation [44]. Besides, grain size, grain boundary and dislocation forests also contribute to the force diversity in ultraprecision machining. Through the investigation of resolved shear stresses, we suppose that the activating sequence of different slipping systems might be another reason to explain the cutting force fluctuation during rotary cutting of titanium alloys with a lamellar martensitic structure.

5. Conclusion

Ultraprecision rotary diamond cutting of Ti-6Al-4V alloy with two different orientations of lamellar martensite produced by electropulsing treatment was conducted to investigate the deformation behaviour of the alloy samples. It firstly discussed the resolved shear stress on various slipping or twinning systems from the perspective of a theoretical model and experimental observations. The conclusion of this study can be drawn as follows:

(i)In low speed ultraprecision rotary groove cutting, the average cutting forces slightly decrease from 2.57 N to 2.34 N as the diamond tool moves from the outside to the centre of the original samples. For EPT treated samples, the cutting forces vary with martensitic orientations and the average cutting forces reduce from 3.04 N to 2.35 N with the decreasing of cutting speed. The enhanced cutting force after EPT is induced by the high yield stress of martensite α.

(ii)A geometrical and physical model was proposed for simulation of resolved shear stresses in slipping or twin directions of various deformation planes of the local anisotropic Ti-6Al-4V alloy. The deformation mechanism in region I is supposed to be basal <a> slip with an activated slipping directions of $[11\bar{2}0]$ and $[1\bar{2}10]$, while activation of prismatic plane with slipping directions of $[\bar{2}110]$ and $[1\bar{2}10]$ is the primary deformation mechanism in region III. Moreover, the type of $\{10\bar{1}2\} < 10\bar{1}1 >$ twin might also contributes to the deformation in region III. No Pyramidal <c+a> slip and other types of twinning were activated in the both regions during ultraprecision rotary cutting process.

(iii)Two orientations of martensite in region I and III give rise to a local anisotropic behaviour of titanium alloys, so the average cutting forces are unequal in the two regions. Furthermore, the cutting forces variation is not only affected by α phase sizes, but also influenced by the coordination and competition of diverse slipping directions. The investigation on deformation mechanism of the Ti-6Al-4V alloy is helpful to reveal the influences of microstructures on the cutting force variation in ultraprecision machining.

References

[1] W. Lee, C. Cheung, A dynamic surface topography model for the prediction of nano-surface generation in ultra-precision machining, Int. J. Mech. Sci. 43 (2001) 961-991.

[2] B.L. Lawson, N. Kota, O.B. Ozdoganlar, Effects of crystallographic anistropy on orthogonal micromachining of single-crystal aluminum, J. Manuf. Sci. Eng. 130 (2008) 031116.

[3] W. Lee, H. Wang, C. Chan, S. To, Finite element modelling of shear angle and cutting force variation induced by material anisotropy in ultra-precision diamond turning, Int. J. Mach. Tools Manuf. 75 (2013) 82-86.

[4] S. To, W. Lee, C. Chan, Ultraprecision diamond turning of aluminium single crystals, J. Mater. Process. Tech. 63 (1997) 157-162.

[5] G. Xiao, S. To, E. Jelenković, Effects of non-amorphizing hydrogen ion implantation on anisotropy in micro cutting of silicon, J. Mater. Process. Tech. 225 (2015) 439-450.

[6] M. Lai, X. Zhang, F. Fang, Crystal Orientation Effect on the Subsurface Deformation of Monocrystalline Germanium in Nanometric Cutting, Nanoscale. Res. Lett. 12 (2017) 296.

[7] J.P. Davim, Machining of titanium alloys, Springer, 2014.

[8] R. Khettabi, L. Fatmi, J. Masounave, V. Songmene, On the micro and nanoparticle emission during machining of titanium and aluminum alloys, CIRP J. Manuf. Sci. Tec. 6 (2013) 175-180.

[9] P.J. Arrazola, A. Garay, L.-M. Iriarte, M. Armendia, S. Marya, F. Le Maitre, Machinability of titanium alloys (Ti6Al4V and Ti555. 3), J. Mater. Process. Tech. 209 (2009) 2223-2230.

[10] M. Nouari, H. Makich, Experimental investigation on the effect of the material microstructure on tool wear when machining hard titanium alloys: Ti–6Al–4V and Ti-555, Int. J. Refract. Met. H. 41 (2013) 259-269.

[11] J. Yang, S. Sun, M. Brandt, W. Yan, Experimental investigation and 3D finite element prediction of the heat affected zone during laser assisted machining of Ti6Al4V alloy, J. Mater. Process. Tech. 210 (2010) 2215-2222.

[12] S. Patil, S. Joshi, A. Tewari, S.S. Joshi, Modelling and simulation of effect of ultrasonic vibrations on machining of Ti6Al4V, Ultrasonics. 54 (2014) 694-705.

[13] W. Yip, S. To, Tool life enhancement in dry diamond turning of titanium alloys using an eddy current damping and a magnetic field for sustainable manufacturing, J. Clean. Prod. 168 (2017) 929-939.

[14] W. Yip, S. To, Ductile and brittle transition behavior of titanium alloys in ultra-precision machining, Sci. Reports. 8 (2018) 3934.
[15] X. Ruibin, H. Wu, Study on cutting mechanism of Ti6Al4V in ultra-precision machining, Int. J. Adv. Manuf. Tech. 86 (2016) 1311-1317.
[16] H.B. Wu, S. To, Effects of electropulsing treatment on material properties and ultra-precision machining of titanium alloy, Int. J. Adv. Manuf. Tech. 82 (2016) 2029-2036.
[17] J. Bai, Q. Bai, X. He, Z. Tong, The ultra-precision cutting Titanium alloy (Ti-6Al-4V): Effects on its microstructure and surface mechanical properties, in: Proceedings of the 16th International Conference of the European Society for Precision Engineering and Nanotechnology, EUSPEN, Nottingham, UK, 2016.
[18] B. Venkatesh, D. Chen, S. Bhole, Effect of heat treatment on mechanical properties of Ti–6Al–4V ELI alloy, Mat. Sci. Eng. A. 506 (2009) 117-124.
[19] T. Seshacharyulu, S. Medeiros, W. Frazier, Y. Prasad, Hot working of commercial Ti–6Al–4V with an equiaxed α–β microstructure: materials modeling considerations, Mat. Sci. Eng. A. 284 (2000) 184-194.
[20] Z. Zhang, S. Qu, A. Feng, J. Shen, D. Chen, Hot deformation behavior of Ti-6Al-4V alloy: effect of initial microstructure, J. Alloy. Compd. 718 (2017) 170-181.
[21] W. Zhang, M. Sui, Y. Zhou, D. Li, Evolution of microstructures in materials induced by electropulsing, Micron. 34 (2003) 189-198.
[22] Y. Jiang, G. Tang, C. Shek, Y. Zhu, Z. Xu, On the thermodynamics and kinetics of electropulsing induced dissolution of β-Mg17Al12 phase in an aged Mg–9Al–1Zn alloy, Acta Mater. 57 (2009) 4797-4808.
[23] Y. Zhu, S. To, W. Lee, X. Liu, Y. Jiang, G. Tang, Effects of dynamic electropulsing on microstructure and elongation of a Zn–Al alloy, Mat. Sci. Eng. A. 501 (2009) 125-132.
[24] H. Wang, G. Song, G. Tang, Evolution of surface mechanical properties and microstructure of Ti6Al4V alloy induced by electropulsing-assisted ultrasonic surface rolling process, J. Alloy. Compd. 681 (2016) 146-156.
[25] X. Ye, J. Kuang, X. Li, G. Tang, Microstructure, properties and temperature evolution of electro-pulsing treated functionally graded Ti–6Al–4V alloy strip, J. Alloy. Compd. 599 (2014) 1-9.
[26] Y. Lou, H. Wu, Improving machinability of titanium alloy by electro-pulsing treatment in ultra-precision machining, Int. J. Adv. Manuf. Tech. 93 (2017) 2299-2304.
[27] T. Ahmed, H. Rack, Phase transformations during cooling in α+ β titanium alloys, Mat. Sci. Eng. A. 243 (1998) 206-211.
[28] S. Leuders, M. Thöne, A. Riemer, T. Niendorf, T. Tröster, H. Richard, H. Maier, On the mechanical behaviour of titanium alloy TiAl6V4 manufactured by selective laser melting: Fatigue resistance and crack growth performance, Int. J. Fatigue. 48 (2013) 300-307.
[29] S. Roy, S. Suwas, S. Tamirisakandala, D.B. Miracle, R. Srinivasan, Development of solidification microstructure in boron-modified alloy Ti–6Al–4V–0.1 B, Acta Mater. 59 (2011) 5494-5510.
[30] D. Banerjee, J. Williams, Perspectives on titanium science and technology, Acta Mater. 61 (2013) 844-879.
[31] S.R. Agnew, Ö. Duygulu, Plastic anisotropy and the role of non-basal slip in magnesium alloy AZ31B, Int. J. Plasticity. 21 (2005) 1161-1193.
[32] Z. Wu, W. Curtin, The origins of high hardening and low ductility in magnesium, Nature. 526 (2015) 62.
[33] W. Hutchinson, M. Barnett, Effective values of critical resolved shear stress for slip in polycrystalline magnesium and other hcp metals, Scripta Mater. 63 (2010) 737-740.
[34] H. Li, D. Mason, T. Bieler, C. Boehlert, M. Crimp, Methodology for estimating the critical resolved shear stress ratios of α-phase Ti using EBSD-based trace analysis, Acta Mater. 61 (2013) 7555-7567.
[35] S.N. Melkote, R. Liu, P. Fernandez-Zelaia, T. Marusich, A physically based constitutive model for simulation of segmented chip formation in orthogonal cutting of commercially pure titanium, CIRP Ann. 64 (2015) 65-68.
[36] X. Zhang, R. Shivpuri, A. Srivastava, Role of phase transformation in chip segmentation during high speed machining of dual phase titanium alloys, J. Mater. Process. Tech. 214 (2014) 3048-3066.

[37] Y. Wang, J. Huang, Texture analysis in hexagonal materials, Mater. Chem. Phys. 81 (2003) 11-26.
[38] A. Kelly, K.M. Knowles, Crystallography and crystal defects, Second ed., John Wiley & Sons, 2012.
[39] H. Matsumoto, H. Yoneda, K. Sato, S. Kurosu, E. Maire, D. Fabregue, T.J. Konno, A. Chiba, Room-temperature ductility of Ti–6Al–4V alloy with α′ martensite microstructure, Mat. Sci. Eng. A. 528 (2011) 1512-1520.
[40] J. Gong, A.J. Wilkinson, Anisotropy in the plastic flow properties of single-crystal α titanium determined from micro-cantilever beams, Acta Mater. 57 (2009) 5693-5705.
[41] G.G. Yapici, I. Karaman, Z.-P. Luo, Mechanical twinning and texture evolution in severely deformed Ti–6Al–4V at high temperatures, Acta Mater. 54 (2006) 3755-3771.
[42] G. Wulf, High strain rate compression of titanium and some titanium alloys, Int. J. Mech. Sci. 21 (1979) 713-718.
[43] T. Britton, H. Liang, F. Dunne, A. Wilkinson, The effect of crystal orientation on the indentation response of commercially pure titanium: experiments and simulations, in: Proceedings of the Royal Society of London A: Mathematical, Physical and Engineering Sciences, The Royal Society, 2010, pp. 695-719.
[44] S. Sun, M. Brandt, M. Dargusch, Characteristics of cutting forces and chip formation in machining of titanium alloys, Int. J. Mach. Tools Manuf. 49 (2009) 561-568.